

Sensor and Simulation Notes

Note 550

25 February 2010

Energy Patterns of the Prototype-Impulse Radiating Antenna (IRA)

D. V. Giri

Pro-Tech, 11-C Orchard Court, Alamo, CA 94507-1541

Dept. of Electrical & Computer Engineering, Univ. of New Mexico, Albuquerque, NM 87131

and

F. M. Tesche

EMConsultant, 1519 Miller Mountain Road, Saluda, NC 28773

Holcombe Dept. of Electrical and Computer Engineering

College of Engineering & Science, 337 Fluor Daniel Building

Box 340915, Clemson, SC 29634-0915

Abstract

A question that often comes up in the context of an IRA is “how is the transient energy from the pulser radiated in space”? Of course the electromagnetic fields (both E and H), the power density and the energy density have their maximum on the boresight. Power pattern is a well-defined frequency domain concept, but it is a cumbersome descriptor for hyperband antennas such as an IRA because of the multitude of frequencies involved. In this note we explore the concept of an energy pattern which holds good both in time and frequency domains. An energy pattern is useful in visualizing where the transient energy provided to the IRA is going. It is further noted that the energy and power patterns are identical for a CW antenna, while they can be vastly different for pulsed antennas.

1. Introduction

An easy way to remember the performance parameters of an antenna is through an acronym “BRIDGE”. The individual letters denote:

- Beamwidth
- Radiation pattern
- Input impedance
- Directivity
- Gain
- Effective area

All of these parameters are well defined in the frequency domain, and are functions of frequency. In the context of pulsed antennas where many frequencies are simultaneously fed into the antenna, the use of frequency dependent parameters is useful, but cumbersome.

Let us consider a reflector type of an IRA as an example of a hyperband [1] antenna [2, 3,4]. The radiation pattern of an IRA is a strong function of frequency as reported in [5]. The lower frequencies of the input pulse have lower gain and large beamwidths, while the higher frequencies have a higher gain and smaller beamwidths. In the next section, we consider an *energy pattern* of the IRA which is a simple and unique descriptor. It is indicative of how the input energy is radiated into all of space.

2. Energy Pattern

Let us denote the energy pattern of the IRA by $U(\theta, \phi)$ in the far field or Fraunhofer zone. This quantity is measured in Joules/steradians. Figure 1 shows the geometry and Cartesian and spherical sets of coordinates with origin at the center of the radiating aperture. The diameter and the focal length of the reflector are denoted by D and F . The Fraunhofer zone is known to begin at an axial distance given by [6]

$$r_{far} = \frac{D^2}{2c\tau_{mr}} \quad (1)$$

where c is the speed of light and τ_{mr} is the maximum rate of rise of the voltage wave launched onto the reflector, which is not necessarily the rate of rise of the transient source waveform.

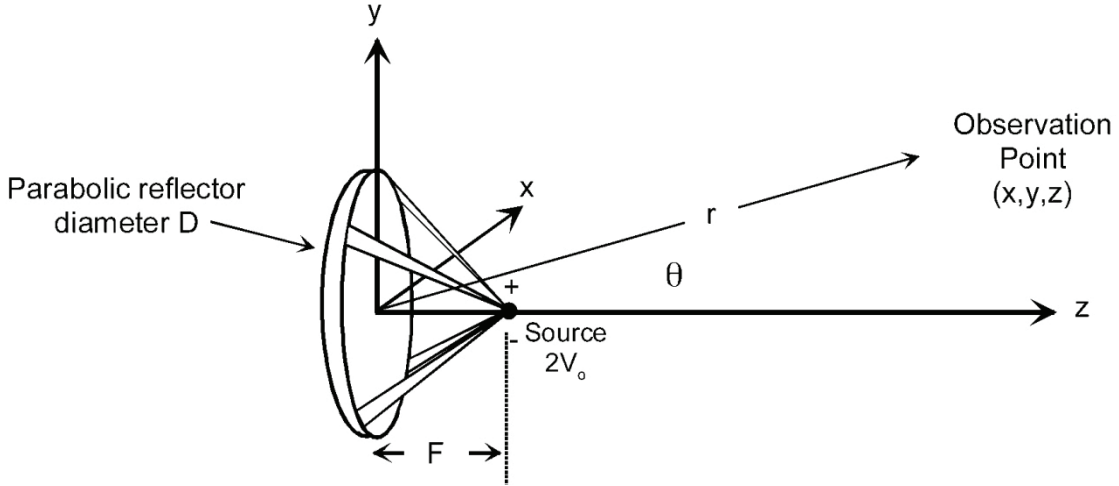


Figure 1. The IRA geometry and coordinate system.

Let $\vec{E}_f(R, \theta, \phi, t)$ and $\tilde{\vec{E}}(R, \theta, \phi, \omega)$ denote the far electric field at an arbitrary location in time and frequency domains respectively. The energy pattern can be defined as

$$U(\theta, \phi) = \frac{1}{Z_0} \int \left| \vec{E}_f(r, \theta, \phi, t) \right|^2 r^2 dt = \frac{1}{2\pi Z_0} \int \left| \tilde{\vec{E}}(r, \theta, \phi) \right|^2 r^2 d\omega$$

(Joules/steradian) (2)

Note that equation (2) represents an energy density and not the total radiated energy. In equation (2), Z_0 is the characteristic impedance of free space and the value of r needs to be in the far field satisfying equation (1). It is noted that energy content of a signal is the same whether one computes it in time domain or frequency domain, as per Parseval's Theorem [7]. It is also observed while the electromagnetic fields depend on the radial distance r , but the energy pattern in the far field is independent of r , simply because the electric field is falling off like r . We can re-write equation (2), in short hand notation as

$$U = \int_0^\infty r^2 \frac{[\vec{E}(t)]^2}{Z_0} dt \quad (\text{Joules /steradian}) \quad (3)$$

In equation (3), $\vec{E}(t)$ denotes the total electric field or the vector sum of all non-zero components. At an arbitrary point (r, θ, ϕ) in the far field, the electric field has a vanishing radial field, and there are only θ and ϕ components. The usual relationships between the rectangular and spherical components are applicable here, if one chooses to compute the Cartesian complements of electric field.

$$\begin{aligned}
E_r &= 0 \\
E_\theta &= E_x \cos(\theta) \cos(\varphi) + E_y \cos(\theta) \sin(\varphi) - E_z \sin(\theta) \\
E_\varphi &= -E_x \sin(\varphi) + E_y \cos(\varphi) \\
E_x &= E_\theta \cos(\theta) \cos(\varphi) - E_\varphi \sin(\varphi) \\
E_y &= E_\theta \cos(\theta) \sin(\varphi) + E_\varphi \cos(\varphi) \\
E_z &= -E_\theta \sin(\theta)
\end{aligned} \tag{4}$$

The square of the magnitude total electric field in time domain is given by

$$|\vec{E}(r, \theta, \varphi, t)|^2 = [E_\theta^2 + E_\varphi^2] = [E_x^2 + E_y^2 + E_z^2] \tag{5}$$

Of course, in practice, the integration is equation (3) is carried out over time limited or band limited ranges.

3. Estimation of Far Fields By Aperture Integration Method

The electric field at any arbitrary observation point in the far field can be estimated by the method of aperture integration that takes into account the presence of the feed arms. Initially the field on the aperture plane is computed. The radiated field can then be computed by an integration of the magnetic current (tangential electric field) on the aperture. The relevant equations are given below [8], with reference to Figure 1.

The magnetic current on the aperture is given by

$$\vec{M} = -2 \vec{l}_z \times \vec{E}_{aperture} \tag{6}$$

and the electric field components in terms of the magnetic current on the aperture are given by

$$\begin{aligned}
E_x &= \frac{1}{4\pi} \iint (z - z') M_y \frac{1 + jkr}{r^3} e^{-jkr} dx' dy' \\
E_y &= \frac{1}{4\pi} \iint (z - z') M_x \frac{1 + jkr}{r^3} e^{-jkr} dx' dy' \\
E_z &= \frac{1}{4\pi} \iint [(y - y') M_x - (x - x') M_y] \frac{1 + jkr}{r^3} e^{-jkr} dx' dy'
\end{aligned} \tag{7}$$

From the estimation of all components of the electric field in frequency domain, the total transient electric field is found by Fourier inversion and then used in equation (3) to get the energy pattern.

Some comments about the aperture integration method outlined above are in order.

The aperture integration method for a hole in an infinite screen is quite accurate in the direction of the main beam, but the accuracy deteriorates as the angle θ increases. This is due to the various approximations used to obtain an analytical solution to this problem. In the EM model used here for the dish, the tangential E and H-fields are normally needed over the aperture, and are assumed to be zero elsewhere on the aperture plane away from the dish. We use only the tangential E-field distribution, however, and assume the corresponding TEM value for the tangential H-field (and this results in an equivalent magnetic current of $M = 2 E_a$ over the aperture).

For this idealized aperture source, the radiated field in the E-plane when $\theta =$ (plus or minus) 90 deg is zero due to geometrical projection reasons. In the H plane, the radiated field does not vanish for $\theta =$ (plus or minus) 90 deg, because the equivalent source is radiating in free-space and this observation point is broadside to the magnetic current source. If there were an infinite, perfectly conducting plate in the plane of the aperture, there the field in the H-plane would go to zero at + - 90 deg due to the boundary condition of $E_{tan} = 0$ on the screen. We also observe that the aperture integration model will not give good results on the back-side of the aperture plane. In fact, the radiation pattern from the equivalent sources is the same in the back as in the front.

In summary, the aperture integration model gives good responses in the forward direction, but not in the backward direction. The numerical errors also increase as the observation point approaches the plane of the aperture.

4. Energy Pattern of the Prototype IRA

In this section, we consider the prototype IRA and evaluate its energy pattern. A photograph of this prototype IRA is shown in Figure 2.

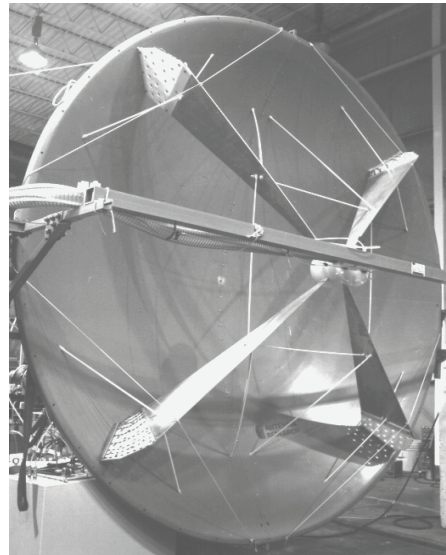


Figure 2. Photograph of the Prototype IRA.

The parameters of the prototype IRA are summarized in Table 1, where we have separately listed the geometry of the reflector and the pulser parameters. Having outlined the salient features of the prototype IRA, we now proceed to compute the radiated fields and the energy pasterns.

The excitation voltage of the IRA is the total plate voltage situated at the focal point of the dish, and is denoted as $V_0(t)$. As outlined in [6], one possible representation of a fast-pulse is given by the expression

$$V_0(t) = V_{peak} (1 + \Gamma) e^{-\beta \left(\frac{t-t_s}{t_r} \right)} \left[0.5 \operatorname{erfc} \left(-\sqrt{\pi} \frac{t-t_s}{t_r} \right) u(-(t-t_s)) + \left[1 - 0.5 \operatorname{erfc} \left(\sqrt{\pi} \frac{t-t_s}{t_r} \right) \right] u(t-t_s) \right] \quad (8)$$

TABLE 1. Antenna and pulser parameters of the prototype IRA

(a) Antenna Details

Parameter	Value
Reflector diameter D	3.66.m
Focal length F	1.22m
F/D	0.33
Number of arms	4
Arm configuration	90 deg
Impedance Z_{in}	200 Ohms
Geometrical factor $f_g = Z_{in}/Z_0$	0.53
Polarization	Linear/Vertical

(b) Pulser Details

Parameter	Value
Peak voltage V_p	$\sim \pm 60 \text{ kV} \sim 120 \text{ kV}$
Peak rate of rise $\left(\frac{dV}{dt} \right)_P$	$\sim 1.2 \times 10^{15} \text{ V/s}$
Maximum rate of rise $t_{mr} = \frac{V_p}{\left(\frac{dV}{dt} \right)_P}$	$\sim 100 \text{ ps}$
Pulse repetition freq PRF	$\sim 200 \text{ Hz}$
Pulse decay time t_d	$\sim 20 \text{ ns}$
Duty cycle $\tau = t_d / PRF$	$\sim 4 \times 10^{-6}$
Peak power $P_{in} = \frac{V_p^2}{Z_{in}}$	$\sim 72 \text{ MW}$
Average power	$\sim 72 \text{ MW} \times 4 \times 10^{-6}$ $\sim 288 \text{ Watts}$

In equation (8), the term $\text{erfc}(\cdot)$ denotes the complementary error function and $u(\cdot)$ is the unit step (Heaviside) function. For the calculations here, the following parameters are used:

- $V_{\text{peak}} = 120 \text{ (kV)}$ (peak value of the transient waveform)
- $\Gamma = 0.006$ (amplitude adjustment factor)
- $\beta = 0.005$ (fall-time coefficient) = rise time / fall time = 100ps / 20 ns
- $\tau_r = 100 \text{ (ps)}$ (waveform rise time)
- $\tau_s = 1.0 \text{ (ns)}$ (time shift)

Figure 3 presents the waveform $V_o(t)$ for late and early times, respectively, and Figure 4 illustrates the time derivative $dV_o(t)/dt$ of the waveform. The spectral magnitude of the waveform is provided in Figure 5.

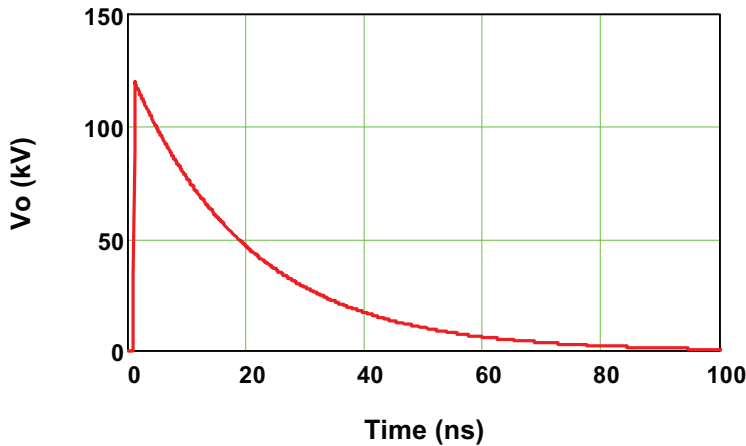


Figure 3. Plot of the excitation waveform $V_o(t)$.

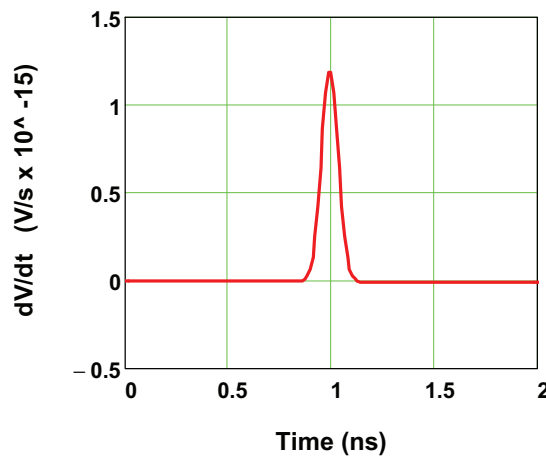


Figure 4. Plot of the time rate of change of the excitation waveform $dV_o(t)/dt$.

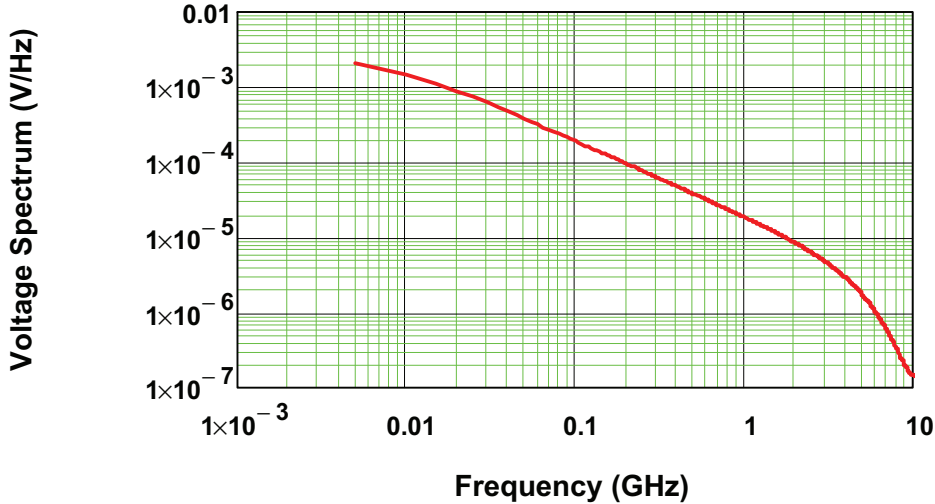


Figure 5. Plot of the spectral magnitude of the excitation waveform.

The calculation of the radiated far-field response of this antenna is done using an aperture integration method, which is described in [9]. The TEM field illuminating the dish is approximated and this forms the aperture field over the dish which is integrated to yield the impulse portion of the response. In addition, the radiation from the feed line currents and the source itself is determined and this provides the pre-pulse contribution to the field.

Overlay plots of the principal components of the transient E-fields for this antenna are presented in Figure 6 for the H-plane and in Figure 8 for the E-plane. Individual plots of these transient waveforms for each angle of observation are plotted on the same scale in Figure 7 and Figure 9 for the H and E-planes, respectively.

As a check of these results, Giri [6] provides the following estimation of the peak value of the impulse portion of the normalized radiated E-field on axis $(\theta, \phi) = 0^\circ, 0^\circ$:

$$rE_{peak} \approx \frac{D}{4\pi c f_g} \left. \frac{\partial V_o}{\partial t} \right|_{peak} \sqrt{2} \text{ (V)} \quad (9)$$

In this expression, $\left. \frac{\partial V_o}{\partial t} \right|_{peak} \approx 1.184 * 10^{15}$ (V/sec) from Figure 4 and $f_g = 1.06$. This provides an estimate of $rE_{peak} \approx 1.534$ MV, which is shown in the figures and agrees well with the present aperture integration calculations.

In these responses, it should be noted that the large impulse-like response occurs only in the boresight direction. It occurs in a very narrow beam around $(\theta, \phi) = 0^\circ, 0^\circ$, and even at a value of $\theta = 1^\circ$ there is a substantial reduction of the peak. Moreover, the waveforms become more dispersed in time as the angle θ increases. It is also noted that the waveforms in the H-plane and in the E-plane are different.

Although the E_x and E_z field components are not plotted here, it suffices to note that they are both either zero or negligible compared with the principal E_y component.

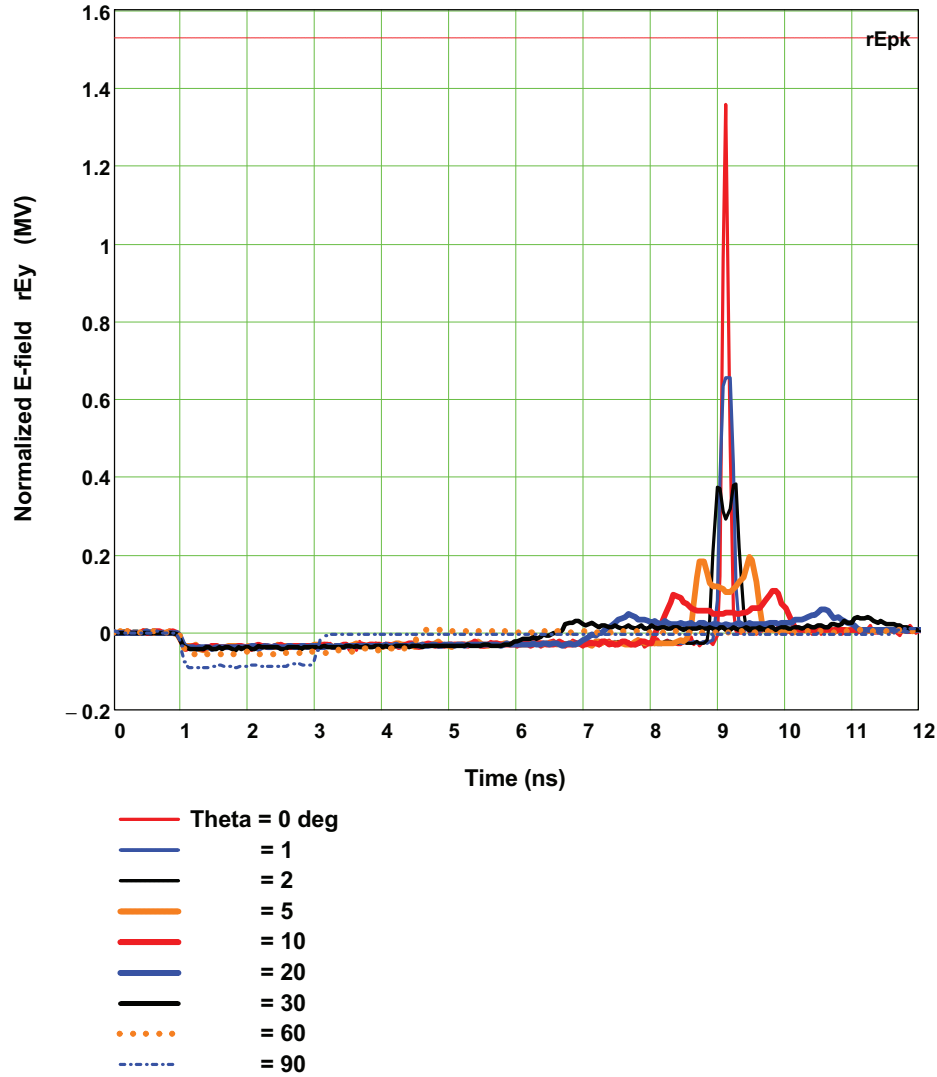


Figure 6. Overlay of the principal (E_y) field components for various values of the angle θ , computed in the horizontal plane (the H-plane) in the far zone of the IRA. (for 120kV/100ps/20ns pulse excitation).

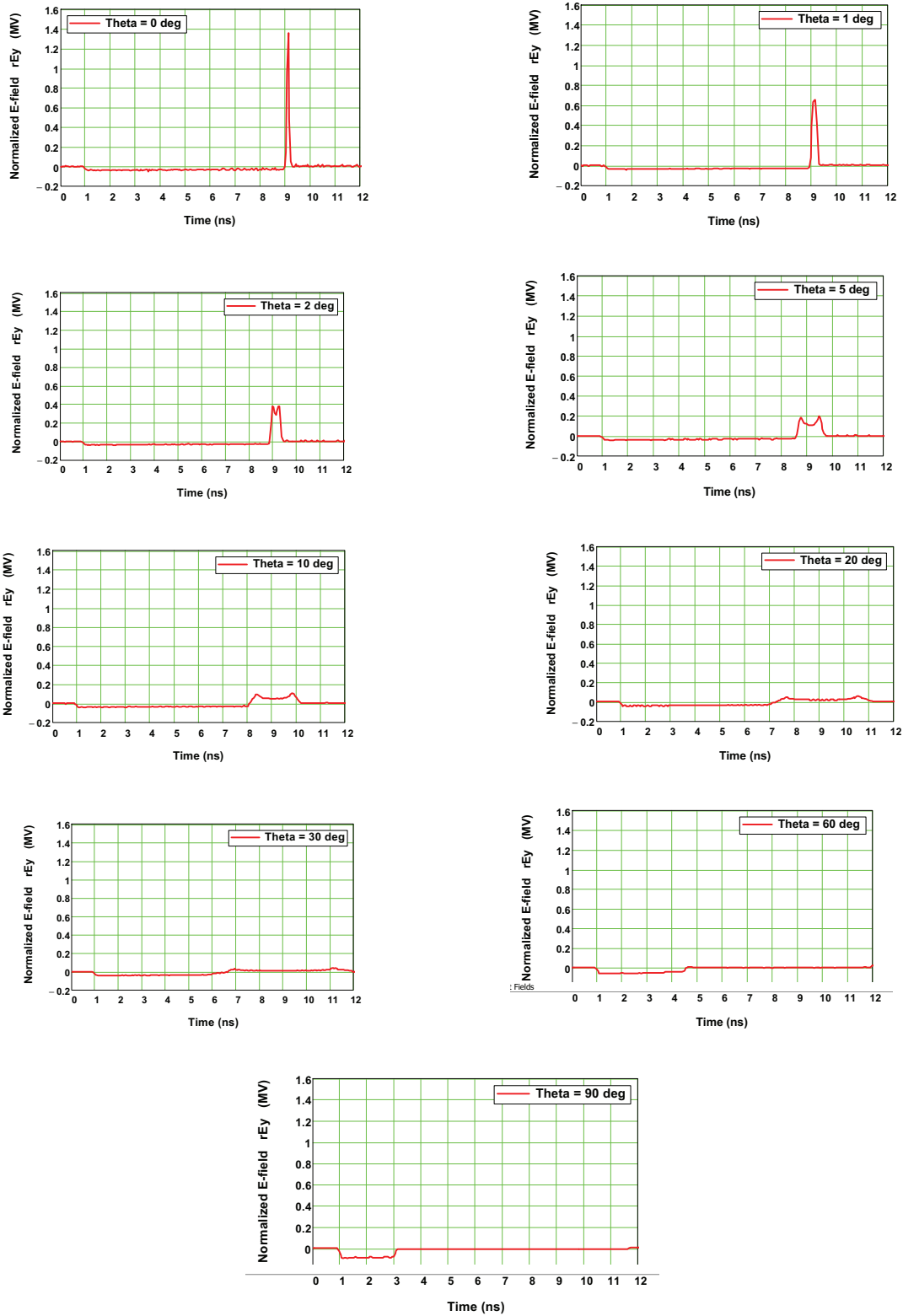


Figure 7. Illustration of the individual principal (E_y) field components in the horizontal plane (the H-plane) in the far zone of the IRA. (120kV/100ps/20ns pulse excitation.)

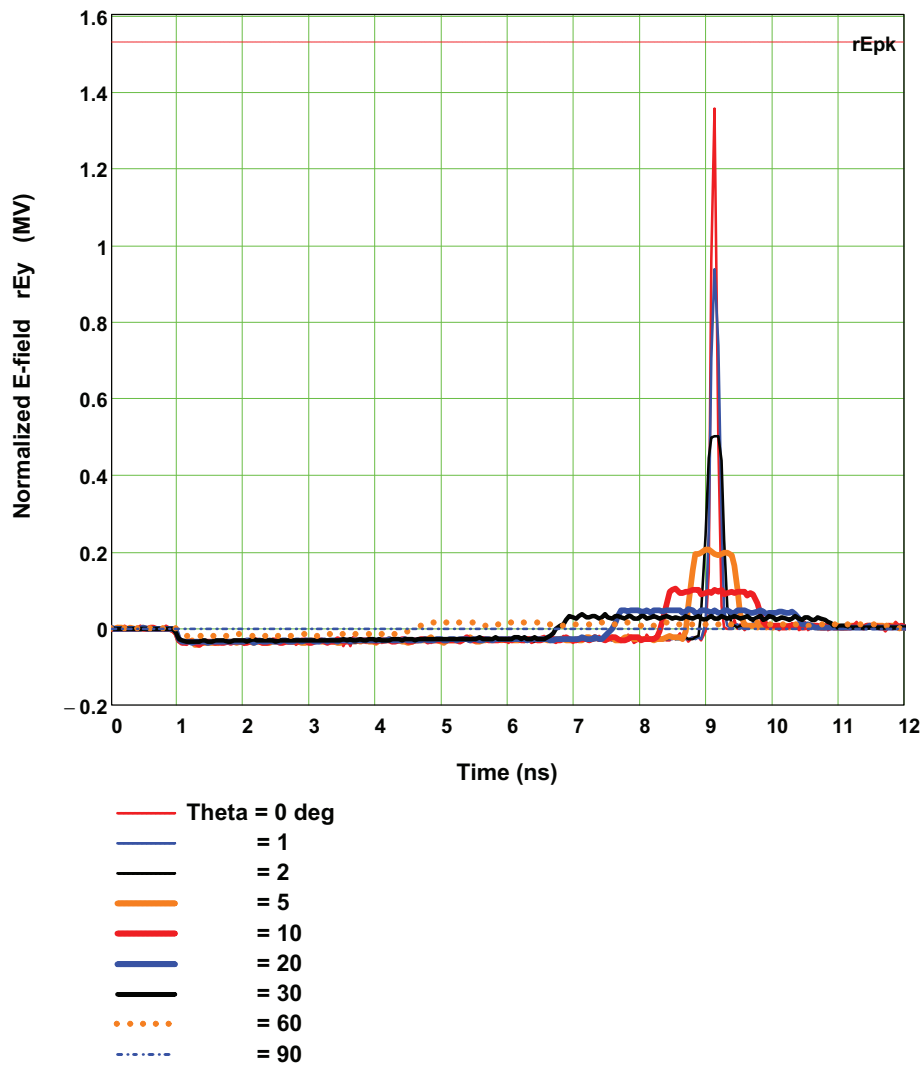


Figure 8. Overlay of the principal (E_y) field components for various values of the angle θ , computed in the vertical plane (the E-plane) in the far zone of the IRA. (for 120kV/100ps/20ns pulse excitation).

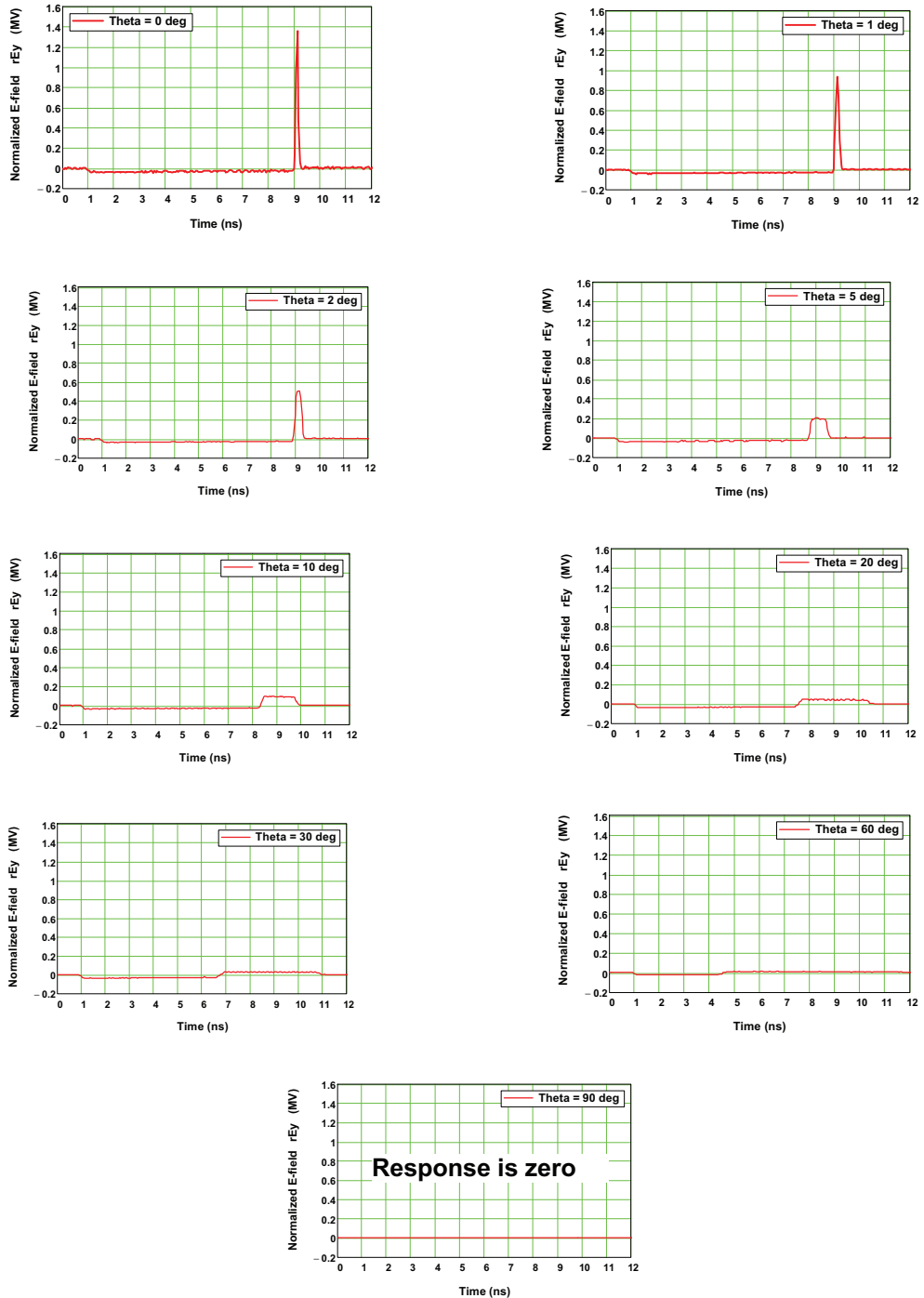


Figure 9. Illustration of the individual principal (E_y) field components in the vertical plane (the E-plane) in the far zone of the IRA. (120kV/100ps/20ns pulse excitation.)

The spectral responses of the E_y field components in the H-plane and E-plane are also of interest. These are plotted as overlay plots for different values of the observation angle θ Figure 10Figure 10 and Figure 11, respectively.

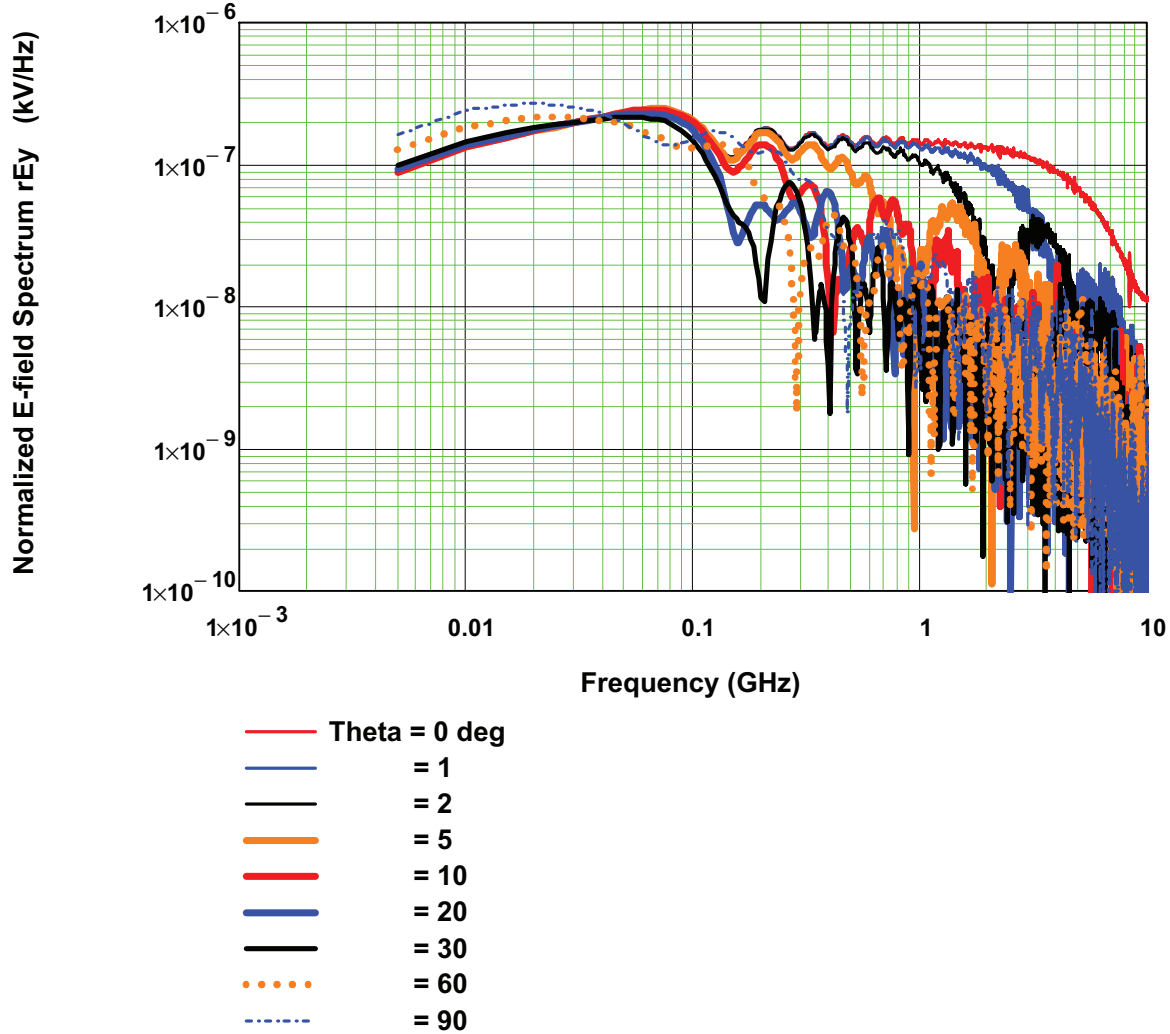


Figure 10. Plot of the spectral magnitudes of the principal (E_y) field components computed in the horizontal plane (the H-plane) in the far zone of the IRA. (120kV/100ps/20ns pulse excitation.)

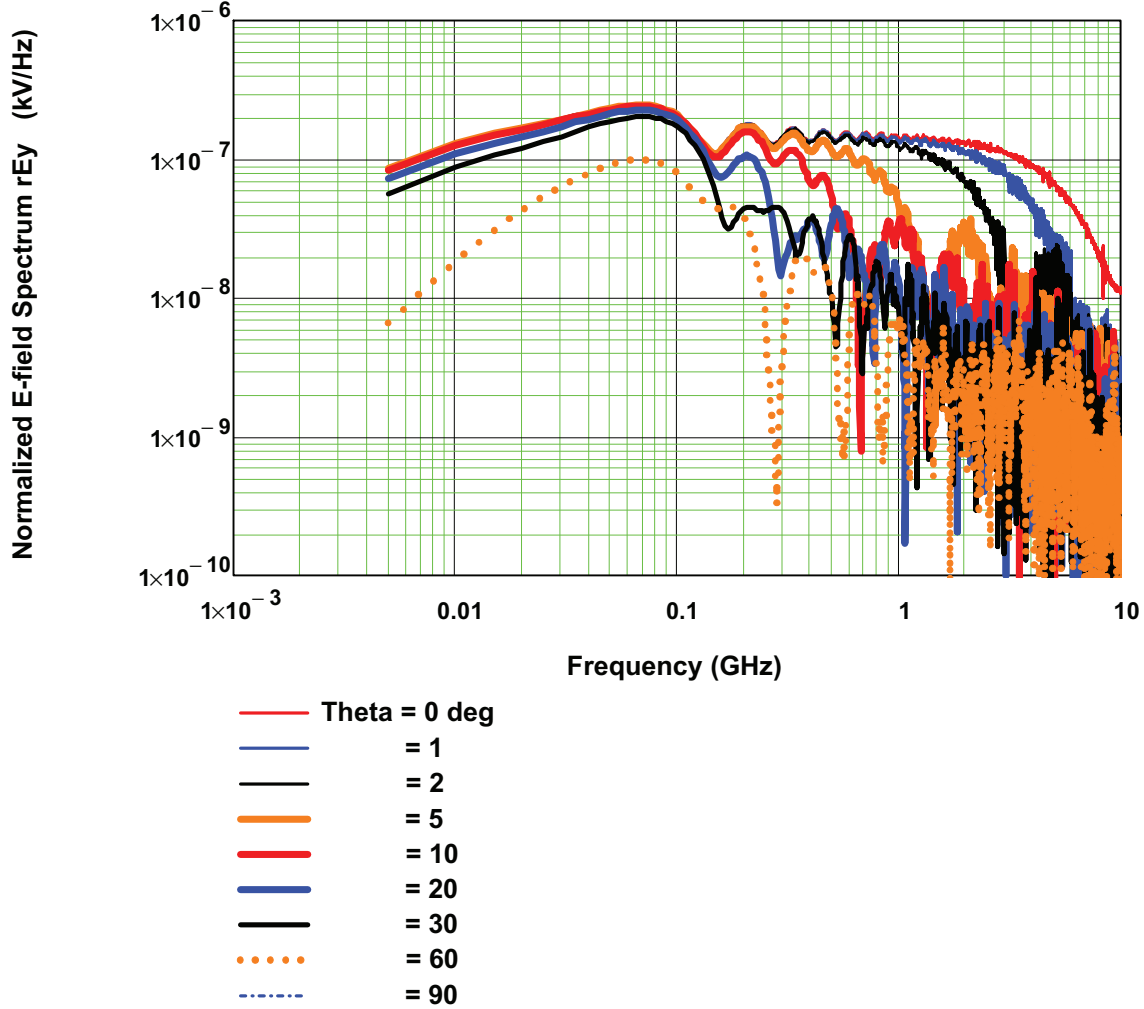


Figure 11. Plot of the spectral magnitudes of the principal (E_y) field components computed in the vertical plane (the E-plane) in the far zone of the IRA. (120kV/100ps/20ns pulse excitation.)

For the driving waveform of Figure 3 into an impedance of 200 Ohms (the net IRA impedance), the total energy delivered to the antenna can be estimated to be

$$U_{in} = \frac{1}{200} \int_0^\infty V_o^2(t) dt \approx \frac{\Delta t}{200} \sum_{k=0}^{N-1} (V_{o,k}^2) = 0.727 \text{ Joules} \quad (10)$$

Of interest is the spatial distribution density (in Joules/steradian) of the radiated energy from the IRA. Equation (3) is evaluated in both of the observation planes by and the results are presented in Figure 12 and Figure 13 for different scales for the y-axis. In this calculation, all

vector components of the calculated E-field are used, even though x and y -components are very small.

It is clear that the IRA sends more energy in the boresight direction. It is important to note that this radiated energy pattern will be different for other excitation sources, because it depends on the frequency content of the excitation voltage.

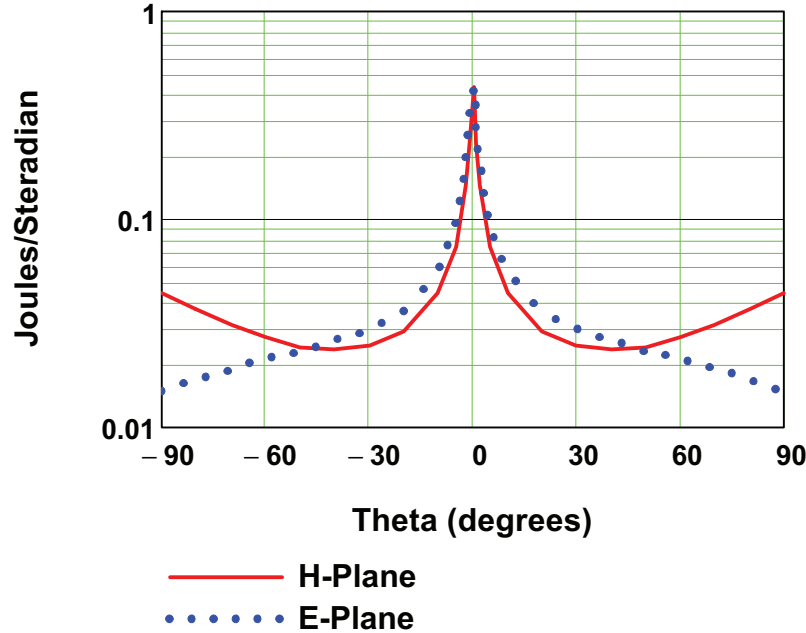


Figure 12. Plot of the radiated energy pattern in the horizontal (H) and vertical (E) planes for the IRA with the voltage excitation of Figure 3. (Log scale on the ordinate.)

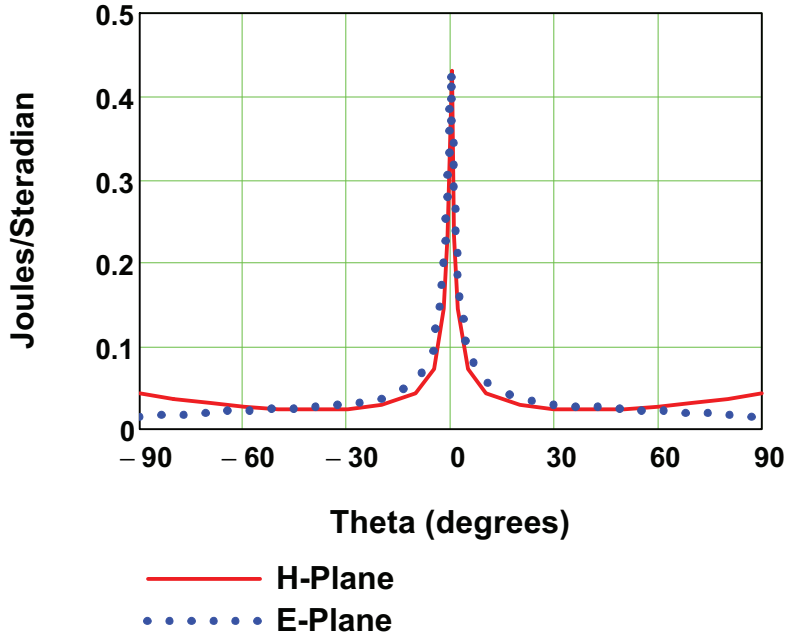


Figure 13. Plot of the radiated energy pattern in the horizontal (H) and vertical (E) planes for the IRA with the voltage excitation of Figure 3. (Linear scale on the ordinate.)

5. Calculations for the prototype IRA with a Damped Sine Wave Excitation

Because the radiated energy pattern depends on the waveform exciting the IRA, it is interesting to consider an alternate excitation function. In this section we examine a damped sine waveform with a center frequency of $f_o = 1$ GHz and exponential damping constant $\alpha = 2 \times 10^8$ (1/sec). The peak amplitude of this waveform is adjusted to provide the same value of the previous pulse waveform, namely $V_{max} = 120$ kV.

Figure 14 illustrates this waveform, and its derivative is shown in Figure 15. The spectral magnitude is provided in Figure 16. For this waveform, the resulting transient responses in the H- and E-planes are shown in Figure 17 and Figure 18, and the spectral responses are in Figure 19 and Figure 20. It is clear that the responses for this excitation are considerably different from those of the fast pulse.

Note that the estimated peak value of $rE_{peak} = 1.009$ MV from equation (9) agrees well with the computed results. It is also worth noting that the low amplitude early time ringing in the waveforms of Figure 17 and Figure 18 is not a FFT problem, but rather, it is the pre-pulse response from the IRA.

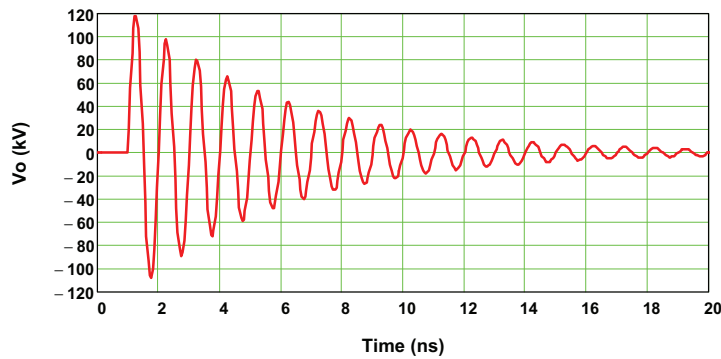


Figure 14. Plot of the excitation waveform $V_o(t)$.

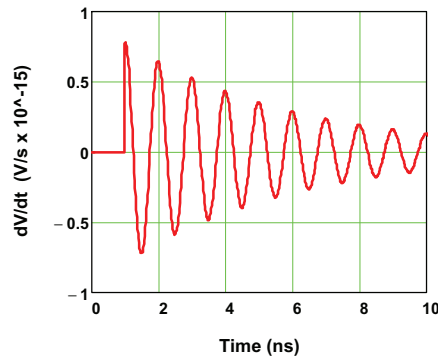


Figure 15. Plot of the time rate of change of the excitation waveform dV_o/dt .

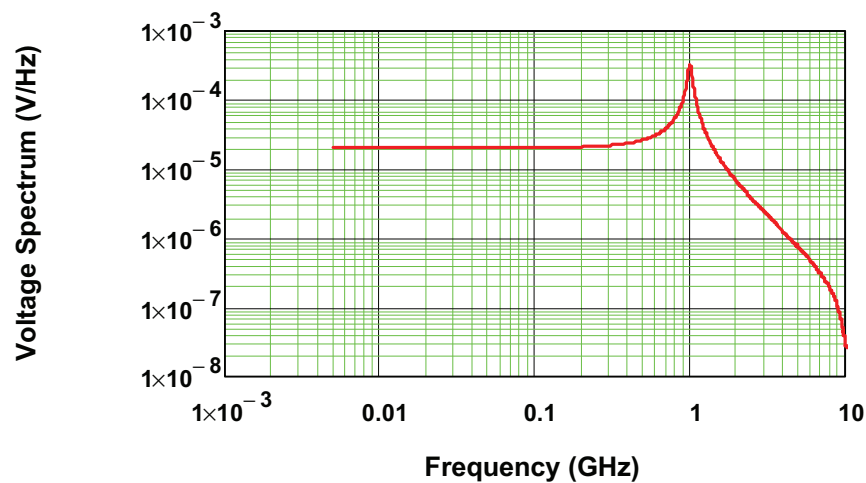


Figure 16. Plot of the spectral magnitude of the excitation waveform.

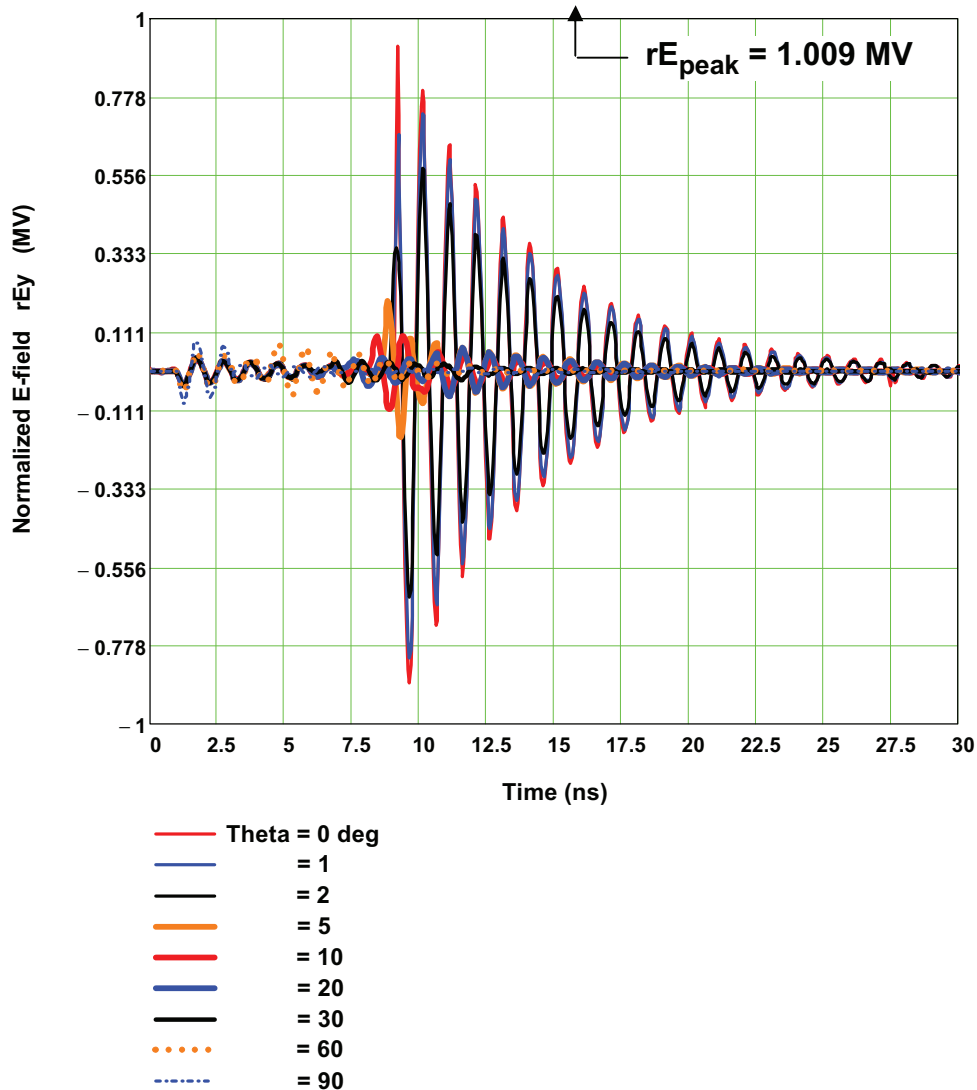


Figure 17. Illustration of the principal (E_y) field component computed in the horizontal plane (the H-plane) in the far zone of the IRA. (120kV/ 1 GHz Damped sinusoidal pulse excitation.)

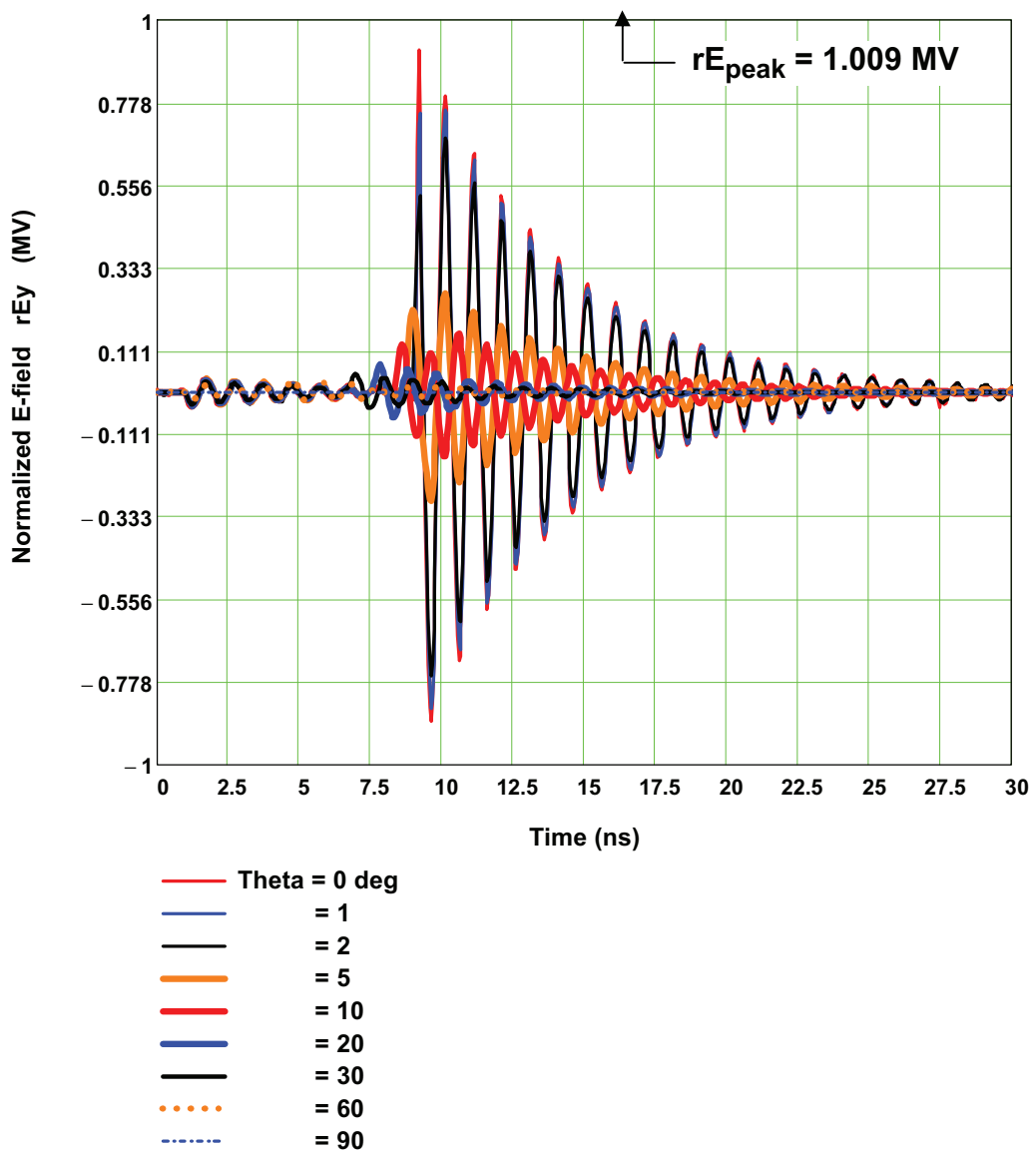


Figure 18. Illustration of the principal (E_y) field component computed in the vertical plane (the E-plane) in the far zone of the IRA. (120 kV/ 1 GHz Damped sinusoidal pulse excitation.)

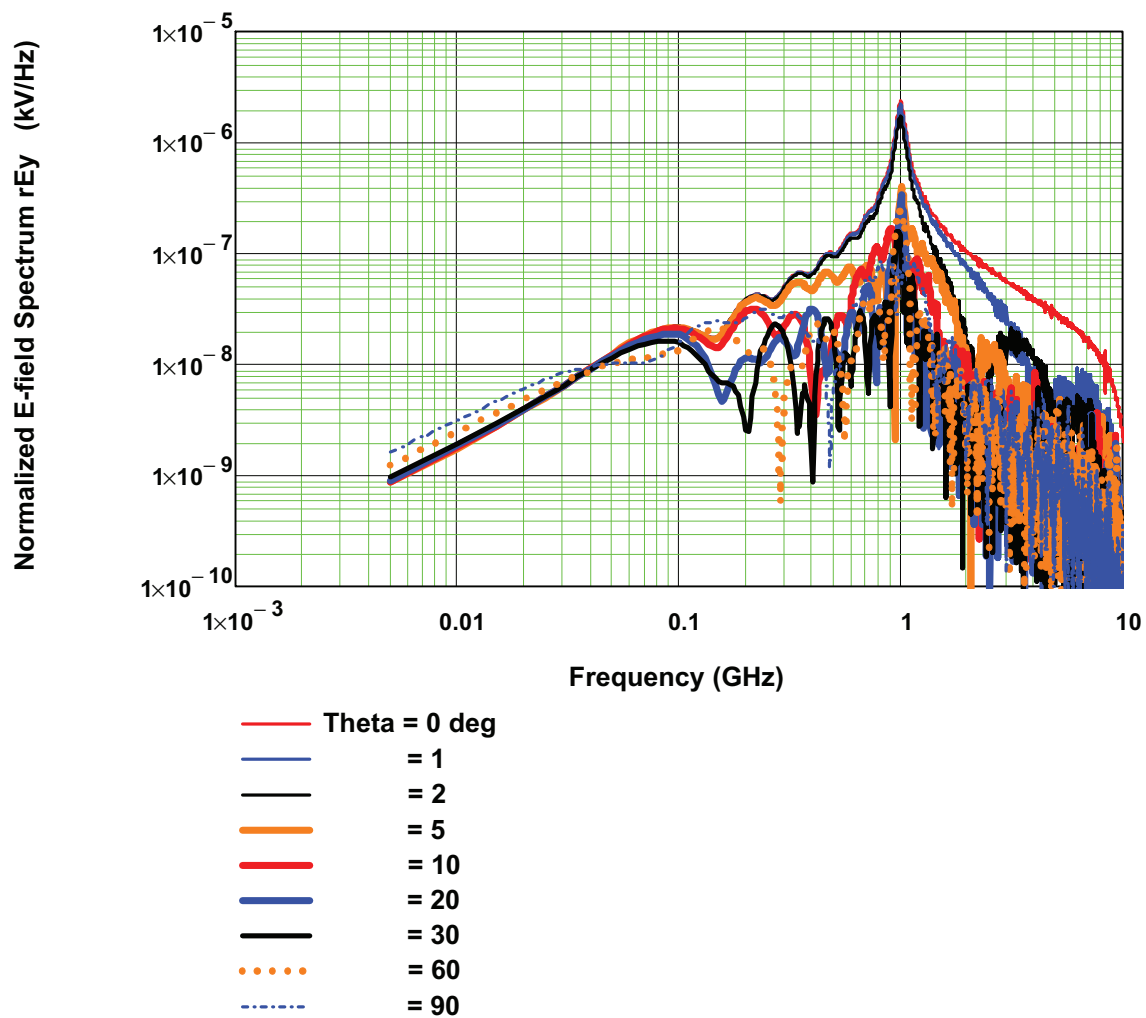


Figure 19. Plot of the spectral magnitudes of the principal (E_y) field component computed in the horizontal plane (the H-plane) in the far zone of the IRA. (120 kV/ 1 GHz Damped sinusoidal pulse excitation.)

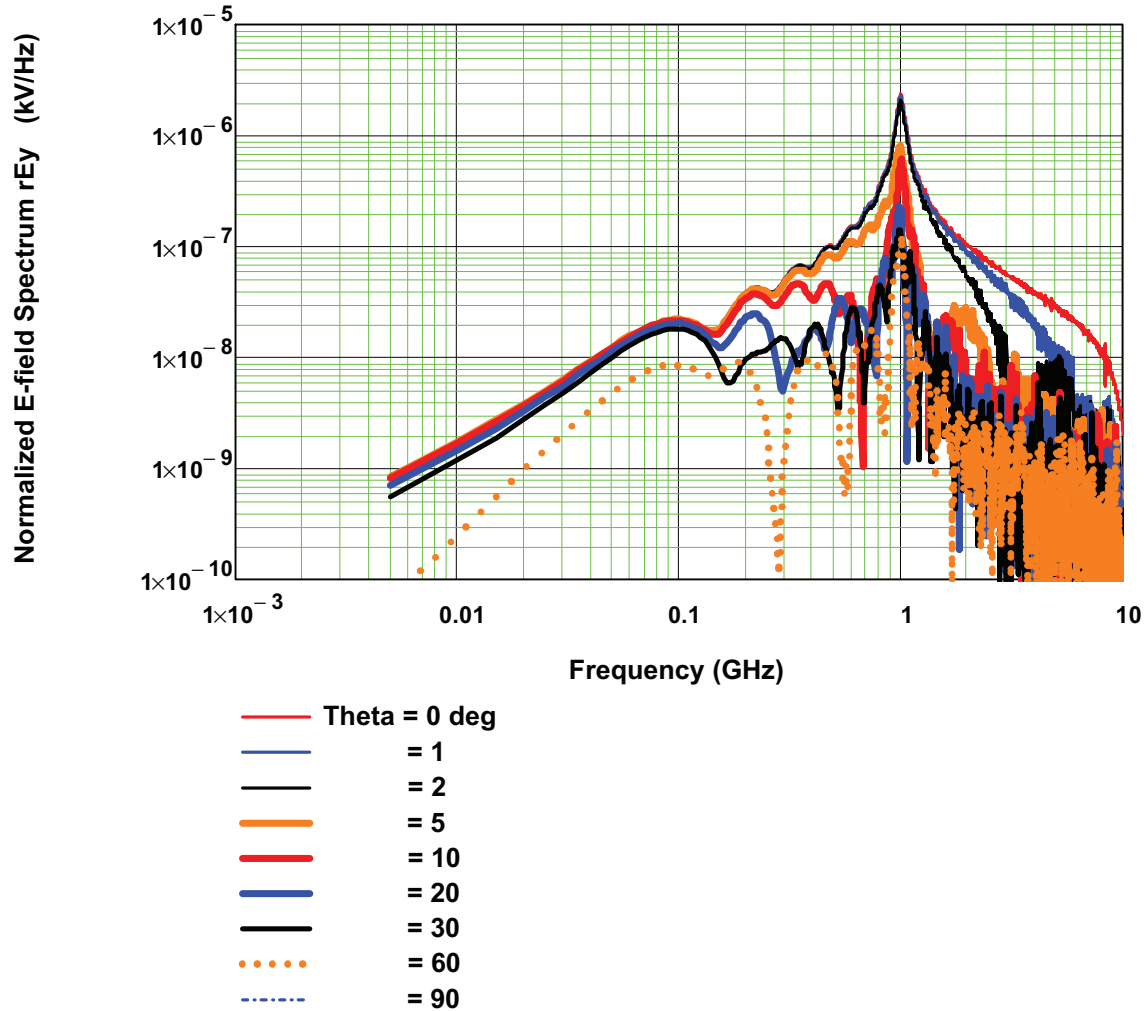


Figure 20. Plot of the spectral magnitudes of the principal (E_y) field component computed in the vertical plane (the E-plane) in the far zone of the IRA. (120 kV/ 1 GHz Damped sinusoidal pulse excitation.)

Figure 21 and Figure 22 present the radiated energy pattern for this damped sine excitation. It is noted that there is more energy radiated in the main beam for this excitation than for the fast pulse. In addition, there are significant side lobe variations in the pattern for off-axis directions. This was not the case for the fast-pulse excitation, because this former excitation contains many frequencies with similar amplitudes and the side lobes tend to wash out in the transient response. This is not the case for the damped sine wave, which has a rather narrow range of significant frequencies in the spectrum.

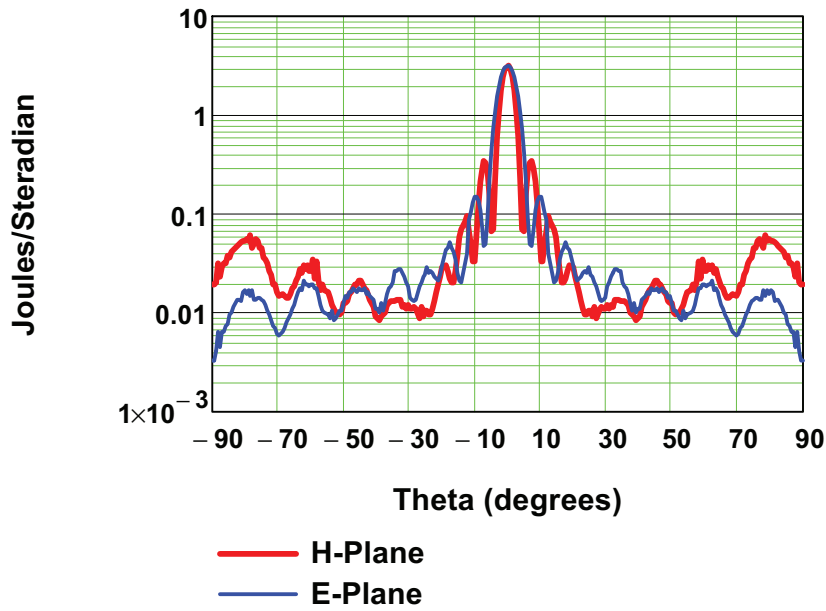


Figure 21. Plot of the radiated energy pattern in the horizontal (H) and vertical (E) planes for the IRA with the damped sinusoidal voltage excitation of Figure 13. (Log scale on the ordinate.)

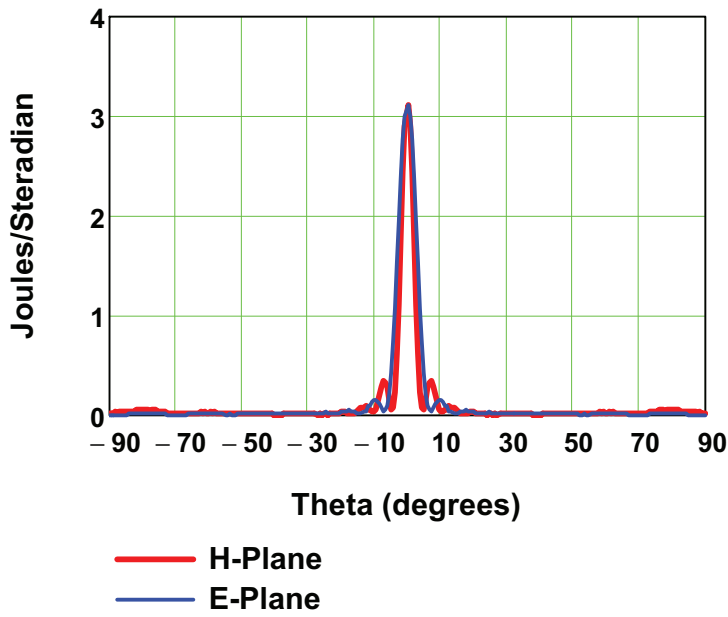


Figure 22. Plot of the radiated energy pattern in the horizontal (H) and vertical (E) planes for the IRA with the voltage excitation of Figure 13. (Linear scale on the ordinate.)

6. Summary

We have explored the concept of energy patterns (measured in Joules/steradian) for a pulsed antenna such as the IRA. In the case of CW antennas, the radiated power and energy patterns are the same. This is not the case for pulsed antennas. The radiated power pattern for a pulsed antenna is a strong function of frequency and can be computed for various frequencies.

In this note, we have considered the prototype IRA and estimated its energy pattern for two different inputs with the same peak voltage amplitude of 120 kV. One input is a fast rising (100ps) - slowly decaying (20ns) mono-polar pulse, while the second is a 1 GHz damped sinusoidal voltage, which is bipolar.

The transient energies of the two input voltages have vastly different frequency components. The fast pulse has frequencies extending from DC to a few GHz, while the damped sinusoidal input is a moderate band source centered at 1 GHz. As a consequence of this, the energy patterns of the same prototype IRA are considerably different for the two input voltages.

In summary, the energy patterns are useful in visualizing where the transient energy provided to the IRA is being radiated in front of the antenna.

7. References

1. D. V. Giri and F. M. Tesche, “Classification of Intentional Electromagnetic Environments (IEME)”, *IEEE Transactions on Electromagnetic Compatibility*, Volume 46, Number 3, August 2004.
2. C. E Baum, “*Radiation of Impulse-Like Transient Fields*,” *Sensor and Simulation Note 321*, 25 November 1989.
3. C. E.Baum and E.G. Farr, “Impulse Radiating Antennas,” in Ultra-Wideband Short Pulse Electromagnetics, edited by H. L. Bertoni et al., pp 139-147, Plenum Press, NY 1993.
4. D. V. Giri, . M. Lehr, W. D. Prather, C. E. Baum, and R. J. Torres, “Intermediate and Far Fields of a Reflector Antenna Energized by a Hydrogen Spark-Gap Switched Pulser”, *IEEE Trans. Plasma Science*, Oct. 2000.
5. K. Sunitha, D. V. Giri, and J. Thomas, “Radiation Patterns of a Reflector Type of Impulse Radiating Antenna (IRA) Relating Time and Frequency Domains,” *Sensor and Simulation Note 545*, 25 October 2009.
6. D. V. Giri, **High-Power Electromagnetic Radiators: Nonlethal Weapons and Other Applications**, published by Harvard University Press, 2004.
7. C. D. McGillem and G. R. Cooper, **Continuous and Discrete Signal and System Analysis**, published by Holt, Reinhart and Winston, Second Edition, 1984.
8. C. A. Balanis, **Antenna Theory Analysis and Design**, John Wiley & Sons, Publishers, Inc., New York, 2005.
9. F. M. Tesche, “Swiss Impulse Radiating Antenna (SWIRA) Characterization”, Report for armasuisse contract 4500314446, August 8, 2005